ARTICLE

High stable CsFAPbIBr perovskite solar cells with dominant bulk recombination at real operating temperatures

Beatriz Romero,*[a] Silvia Delgado, [a] Damian Glowienka, [b] Cheng-Tsung Chang, [c] Gonzalo del Pozo, [a] Belén Arredondo, [a] Diego Martín-Martín, [a] Pedro Contreras [a], and Yulia Galagan, [c]

Mixed-cation mixed halide Perovskite Solar Cells have been characterized in DC at different temperatures (from -20 °C up to 50 °C) and the time evolution of the device efficiency has been assessed using different degradation protocols (indoor and outdoor). The complete planar p-i-n structure is ITO/CuNiO$_x$/PTAA/CsFAPbIBr/PCBM/PEI/Ag. Pristine current-Voltage characteristics barely show hysteresis, at any temperature. Open circuit voltage decreases with temperature at a rate of -1.5 mV/°C, and the obtained PCE temperature coefficient is lower than -0.001 %/K, which is an outstanding value for this emerging photovoltaic technology. Cells have been degraded under different protocols: indoor using different light/dark cycles and outdoor testing in a high temperature and high irradiation location. Cells show no significant decrease of the efficiency after more than 350 h of indoor light cycling and the estimated T$_{80}$ obtained for the sample degraded outdoor under high irradiation and high temperature conditions is ~ 15 days.

Introduction

Perovskite Solar Cells (PSC) are a promising 3rd generation photovoltaic technology very likely to contribute to large scale solar energy production, due to their outstanding PCE, and their compatibility with low-cost, scalable processes, such as inkjet printing or roll-to-roll[1]. In a time frame of ten years, PCE has raised from 3.8 % up to 25.8 %[2]. Never before such progress in PCE has been witnessed in the history of solar cells. Besides, PSC are light, thin, and can be semi-transparent and/or flexible, which make them suitable for special applications such as Building Integrated Photovoltaics (BIPV)[3], or space missions[4].

Regarding material composition, many works are currently focusing on using mixed-cation mixed-halide PSC with the aim of increasing device stability and efficiency. The incorporation of new cations such as Formamidinium (FA) or Cs has proven to increase device stability[5]. On the other hand, the incorporation of Br or Cl increases the energy gap and therefore lowers the absorption spectrum of the active layer material. In addition, some authors have observed that charge recombination is reduced when increasing the Br/I ratio[6]. Regarding the layer structure, p-i-n structures have demonstrated to exhibit lower hysteresis, and better stability than the n-i-p layer structures[7].

On the other hand, other authors have focused on avoiding lead in the perovskite composition due to the high toxicity of this metal, that could hamper the device commercialization Non-toxic inorganic cations like Sn or Ge have been used to substitute Pb[8]. Regarding Hole Transport Layers (HTL), one of the most used materials is SpiroOmetad. However, since this material easily degrades at high operation temperatures, other materials such as polytriarylamine (PTAA) are becoming more popular. PTAA has demonstrated to be a good HTL material for different photovoltaic device configurations, including n-i-p, p-i-n and tandem solar cells[9]. Some authors have already demonstrated a reduction in the charge interface recombination when substituting inorganic oxides, such as CuO$_x$, by PTAA[10,11].

However, in spite of the outstanding progress of PSC, very little attention has been paid to the device performance efficiency close to operating temperatures. The temperature of the cell can easily reach 60-70 °C in high irradiation locations during the summer. Therefore, it is crucial to understand how these conditions affect the efficiency and stability of the cells. Some authors have studied the performance of PSC under simulated temperature and illumination conditions, concluding that PSC efficiency does not significantly change between 25 °C and 50 °C at 1 sun[12]. Other experimental works report a PCE characteristic temperature of -0.08 %/°C for triple-cation PSC[13]. In addition, temperature measurements are a valuable tool for determining the activation energy, E$_a$, from the y-axis intercept of V$_{OC}$ vs temperature. By comparing this activation energy with the energy gap, Tress et al. determined where the main recombination process takes place, either in the bulk or at the perovskite/contact interface[14].

Regarding the stability of PSC, new ISOS protocols have been recently stablished[15], adapting the ones developed in 2011 for Organic Solar Cells[16]. These protocols include light cycling experiments since PSC show two different trends under these conditions. On the one hand, some authors have observed a recovery of the efficiency during the dark period[17], while others

a. Electronic Technology Area, Universidad Rey Juan Carlos, Mostoles 28933, Spain
b. Gdańsk University of Technology, Faculty of Appl. Phys., Narutowicza 11/12, 80-233 Gdańsk, Poland
c. 2National Taiwan University, Dep. of Mat. Sci. and Eng., No.1, Roosevelt Rd, Sect 4, Taipei, 106, Taiwan Address here.

have observed the opposite behaviour, a light-induced enhancement of the efficiency under light soaking[18,19].

In this work, CsFAPbIBr based solar cells have been manufactured and characterized in DC at different temperatures, from -20 °C up to 50 °C. The samples barely show hysteresis, at any scan rate, and the efficiency did not significantly drop under high temperature conditions, yielding a PCE temperature coefficient, T_{PCE} ~ 0. Pristine samples have been degraded using 2h/2h, and 16h/8h light cycling indoor degradation during several days and no significant decay of the efficiency was observed. An outdoor degradation protocol was applied to a cell for 32 days, yielding a T_{80} of around 15 days.

Results and discussion

Solar cells performance at room temperature

The samples needed around 30 minutes light soaking to be fully activated, since pristine *J-V* curves show a pronounced S-shape that is completely removed after the activation process. Fig. 1 shows the evolution of the fill factor (FF) and the efficiency (η) of a fresh device versus light soaking time. As it can be observed, FF increases from 32 % up to 62 %, and efficiency from 6 % up to 12 %. The inset in Fig. 1 shows that the S-shape of the pristine *J-V* curve is removed after 24 minutes of light soaking. Activated devices partially deactivate when stored in dark conditions, as it will be shown in the light cycling degradation experiment at the end of this section.
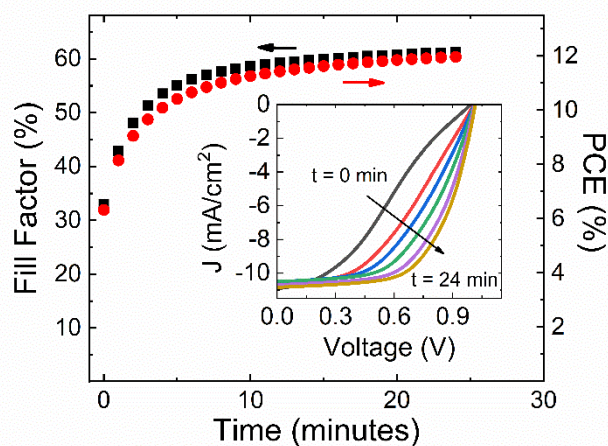

Fig. 1 Evolution of FF and PCE of a solar cell under light soaking during activation. The inset shows the J-V characteristics recorded at t = 0, 1, 2, 4, 5, 10, and 24 minutes.

Pristine activated *J-V* curves have been recorded for several devices, in forward and in reverse at different scan rates, from 5 mV/s up to 1 V/s. Fig 2. shows an example of the forward and reverse I-V characteristic, measured at 20 mV/s, under 1 sun. The inset shows the Hysteresis Index (HI) defined by expression (1) at varying scan rates (from 5 mV/s up to 1 V/s).

$$HI = \frac{(A_r - A_f)}{Max\,(A_r, A_f)}x100 \qquad (1)$$

Where A_r is the area above the *J-V* curve from V_{OC} to 0 V and A_f is the area above the *J-V* curve from 0 V to V_{OC}.

As it can be observed in Fig 2, the curves barely show hysteresis at 20 mV/s and HI is always lower than 6 % in the chosen scan rate range (see inset of Fig. 2). According to Calado et al.[20,21], hysteresis in PSC appears when two conditions are fulfilled, the presence of a mobile ion distribution across the device and when recombination at the interface (contacts) is the governing mechanism. Since ions are usually present in perovskite devices, our hypothesis is that recombination at the interface is not dominating the overall recombination mechanism at room temperature. This hypothesis will be supported in the next section, with the value of the activation energy obtained from temperature dependence of V_{OC}.
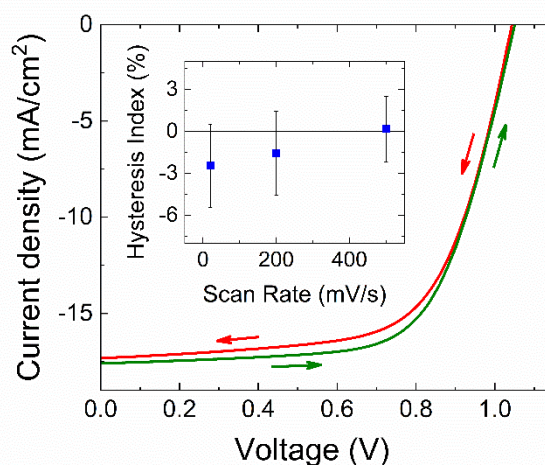

Fig. 2 *J-V* characteristic in forward (green) and reverse (red) measured at 20 mV/s. The inset shows the variation of HI with the scan rate.

A total number of 14 devices have been characterized in DC after being completely activated. The *J-V* curves have been recorded in reverse condition at 20 mV/s at different illumination levels. Table I summarizes the values of the solar cells' parameters at 1 sun.

Table I. Solar cell parameters, J_{SC}, V_{OC}, FF and Efficiency @25 °C and 1 sun. Measurement conditions: 20 mV/s in reverse scan.

J_{SC} (mA/cm²)	V_{OC} (V)	FF (%)	Efficiency (%)
15.25 ± 3.22	1.02 ± 0.05	0.59 ± 0.04	9.43 ± 1.39

J-V curves have been measured at different illumination levels (0.13, 0.25, 0.5 and 1 sun). From the dependence of V_{OC} with light intensity, ideality factor has been extracted, yielding a value of 1.4 ±0.4. As it is well known, it is very common to consider ideality factor as a representation of the dominant recombination process. In perovskite solar cells, the losses from radiative and Auger recombination are rather negligible. It has been already proved that the nonradiative recombination is the dominant recombination mechanism. However, it is still challenging to conclude whether efficiency losses are coming from interface recombination and/or from bulk defects. In general, it is considered that the ideality factor increases when bulk recombination (SRH) dominates. However, if the interface recombination is very high, the ideality factor is not govern by bulk mediated recombination [23]. In these devices, the obtained ideality factor is 1.4, reinforcing the aforementioned hypothesis that bulk recombination is dominating.

Temperature dependence of solar cell performance

The *J-V* characteristic of 6 devices has been measured at different temperatures, ranging from -20 °C up to 50 °C at different light intensities (from 0,13 to 1 sun) in reverse at 20 mV/s. Fig. 3 shows cell parameters vs temperature at 1 sun. As it will be explained in the experimental section, efficiencies are underestimated, since the irradiation intensity reaching the cells is around 15 % lower than 1 sun, due to reflections and absorption losses in the temperature stage quartz window. As it can be observed, J_{SC} barely changes with temperature, indicating that photogeneration/extraction does not significantly change within this temperature range. On the other hand, V_{OC} decreases with temperature at a rate of 1.5 mV/K. This decrease is lower than the one occurring in devices based on other mature technologies, such as silicon (2.3 mV/°K), due to its lower bandgap, or GaAs (2-2.2 mV/°K). To quantify the high temperature effect on the efficiency, T_{PCE} has been calculated. T_{PCE} is equal to the change in PCE over the change in temperature, normalized with respect to the PCE at room temperature. The standard values for silicon or GaAs based cells are -0.4 and -0.3 %/K respectively. The obtained value for these perovskite devices was -0.0004 %/K. This is a remarkable temperature performance, which makes these kind of PSC good candidates to perform under high temperature conditions.

The inset of figure 3b shows the extrapolation of V_{OC} at 0 K (activation energy, E_a), at different irradiation intensities. The obtained values for E_a range between 1.59 eV at 1 sun and 1.65 eV at 0.13 suns, which are very similar to the band gap energy (E_g) of this perovskite material, ~ 1.58 eV, obtained from EQE measurements. According to Tress et al, an E_a similar to E_g supports that the main recombination process takes place in the bulk and neither via tail states, nor interface recombination[14]. This is in good agreement with the previous assumption of neglectable recombination at the interface in these devices at 25 °C.

Fig. 4 shows the ideality factor at different temperatures, calculated from the slope of V_{OC} vs light intensity. At open-circuit conditions, the generation and recombination processes are compensated, and no net current is extracted from the device. Therefore, the transport processes can be omitted. We clearly see that the ideality factor is not significantly changing with a value around 1.4 in the temperature range from 50 °C to 10 °C. This value again suggests that bulk recombination is governing the whole recombination mechanisms. At the lowest temperature, the ideality factor drops down to 1.2. This significant drop is consistent with an increase of the interface recombination process. However, this conclusion is not straightforward, since the perovskite defect density at the interfaces is not to be affected by temperature, but rather the phase of the material. The phase transition of perovskite material from tetragonal to orthorhombic starts to develop at around 0 °C and fully transfers at -40 °C [24]. On the other hand, the carrier thermal energy and the energy barrier between transport layers may depend on the temperature, which could enhance interface recombination at low temperatures.

Fig. 5 shows the dependence of FF on light intensity at different temperatures. At high light intensities (1 sun) FF changes from 64 % (at 50 °C) to 50 % (at -20 °C), which is a 14 % drop, whereas at low light intensity, 0.13 suns, the drop is from 71 %, at 50° C to 67 % at -20 °C (only 4 % drop). We have presented a similar change of FF in devices with the same configuration [23]. In this work we have also found that at low temperatures, when interface recombination becomes to be relevant, the drop of the FF with light intensity is more pronounced, as it can be seen in Fig. 5 for temperatures below 0 °C. For temperatures above 0 °C the slope of FF with light intensity decreases, confirming that bulk recombination is significantly dominant.
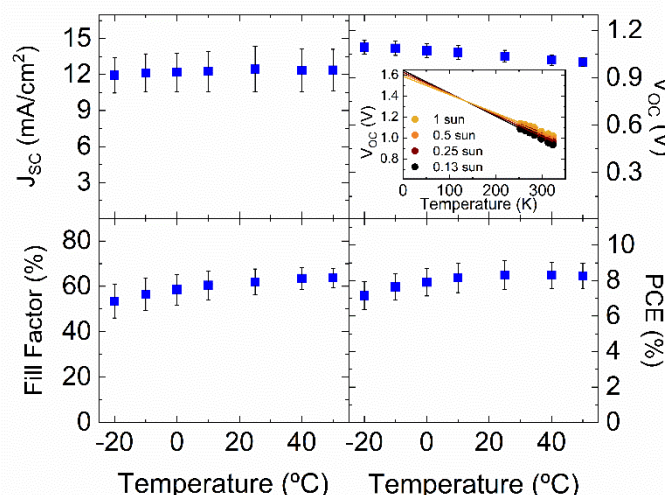

Fig. 3 Solar cell parameters, J_{SC}, V_{OC}, FF and PCE vs. temperature. Six devices have been measured for statistics. The inset in figure b shows V_{OC} vs temperature at different irradiation levels. The intercept with y-axis indicates the activation energy, E_a.
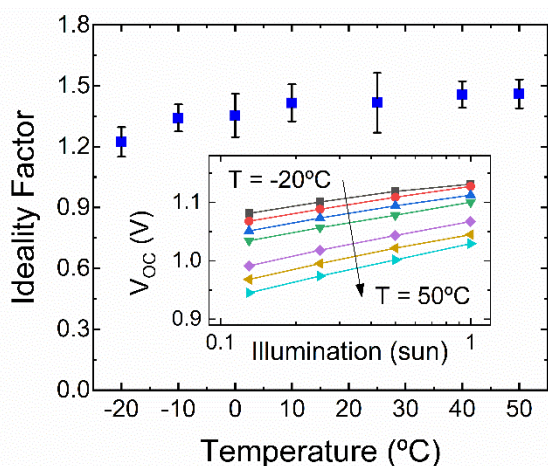
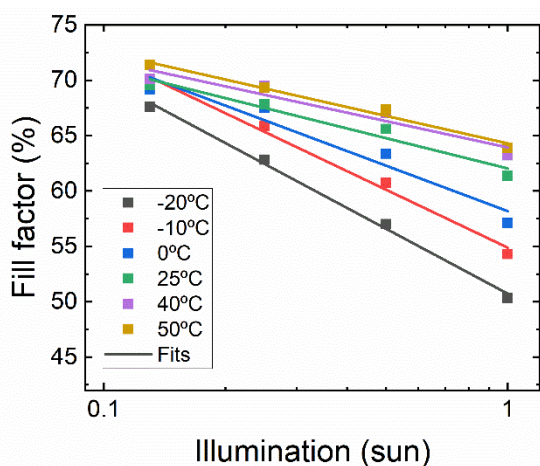Fig.4 Ideality factor vs temperature obtained from the dependence of V_{OC} with irradiation level (see inset).

Fig.5 Fill Factor vs light intensity at different temperatures, from -20 °C to 50 °C.

Degradation characterization

We have also performed an indoor degradation experiment using a light cycling protocol (ISOS-LC1)[15]. The experiment started with cycles of 2h/2h (light/dark). As it can be observed in the inset of Fig. 6, during the 2 hours of darkness, especially in the first periods, there was a drop in the efficiency related to a deactivation of the cells. This decay is recovered during the next 2 h of light. This deactivation is reduced with the number of cycles. This reversible loss of efficiency during the dark period has been previously observed by other authors[18,19]. After more than 350 hours of 2/2 light cycling, devices show no appreciable drop of the efficiency. Therefore, to accelerate the degradation, the light/dark cycle was increased to 16 h light/8 h dark. After six additional days, the efficiency did not drop significantly, as it can be seen in the figure. The drop observed during the first three days of the new 16h/8 h cycle was due to an unexpected

displacement between the sample and the solar simulator, that was corrected as soon as it was detected. In conclusion, there was no significant drop of the efficiency after almost 600 h of light indoor cycling (~ 24 days).
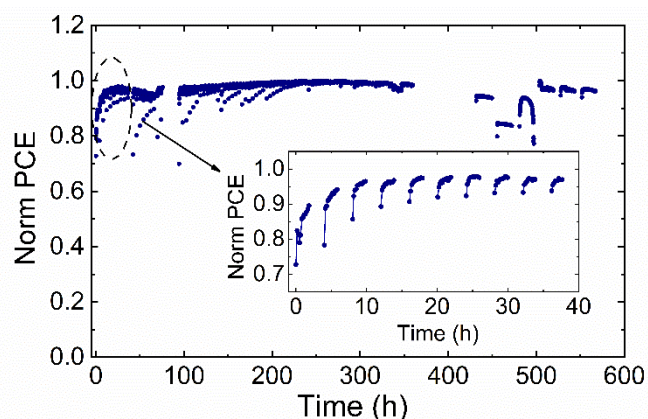

Fig. 6 Evolution of the normalized PCE for the light cycling experiment in indoor conditions. Cycle was 2h light/2h dark during the first 350 h and 16h light/8h dark during the next 144 h. The inset shows the evolution of PCE during the first 10 cycles (40 h).

A second degradation experiment was carried out outdoors. The cell was placed on a sun tracker for 32 days in Madrid (GPS: 40.334, -3.883) from the 10th of June to the 12th of July 2022. During this period the average temperature was 26 °C being the maximum and minimum 39 °C and 12 °C, respectively. The average relative humidity was 34 % and the total global irradiation was 256 kWh/m². During the experiment there were two periods of time with no data recorded due to a problem in the data acquisition system. Since T_{80} occurred during one of these periods, we have linearly interpolated the efficiency in that period. From the interpolation of the efficiency evolution, the estimated T_{80} was > 15 days, which is a remarkable value for this technology, given the extreme temperature and irradiation conditions.
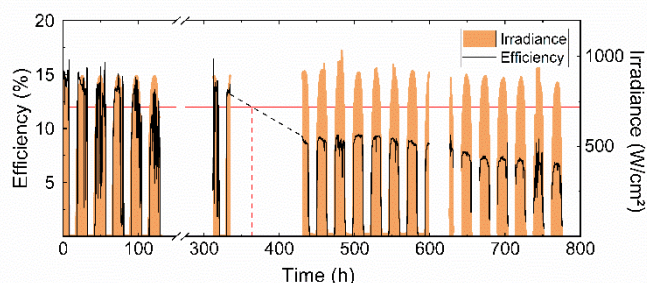

Fig.7 Evolution of the efficiency and irradiance in the outdoor degradation experiment. Dotted line has been interpolated to estimate T_{80}

Experimental

Fabrication

3x3 cm ITO substrates were etched using 37% hydrochloric acid (HCl) diluted in deionized water in 1:10 volumetric ratio. The active part of the ITO was protected using scotch tape and zinc powder (Fisher Chemical) was used to enhance the etching process. Further, the ITO substrates were cleaned using 10 min sonication at each step with soap solution in water, mixture of 10 mL of ammonia and 10 mL H_2O_2, deionized water, methanol and then finally isopropanol. Subsequently, the substrates were dried with N_2, and cleaned for 15 minutes in plasma oven on high power.

Commercial nickel nitrate hexahydrate $(Ni(NO3)2*6H_2O)$ (98%, Alfa Aesar), copper (II) nitrate trihydrate $(Cu(NO_3)2*3H_2O)$ (99%, Sigma Aldrich), 2-methoxyethanol (99%, Alfa Aesar), acelyacetone (Kanto Chemicals), poly(triaryl amine) (PTAA) (Solaris L), lead iodide (PbI_2) (99.99%, Alfa Aesar), formamidinium iodide (FAI) (GreatCell Solar), Cesium bromide (CsBr) (99.999%, Alfa Aesar), dimethylformamide (DMF) solvent (99.8%, Sigma-Aldrich), dimethyl sulfoxide (DMSO) solvent (99.9%, Sigma-Aldrich), chlorobenzene (CB) (Sigma-Aldrich), isopropanol (IPA) (Sigma-Aldrich), toluene (extra dry, Sigma-Aldrich), [6,6]-phenyl C61 butyric acid methyl ester (PCBM) (99%, Solenne), polyethyleneimine (PEI) (branched, Average Mn 10k, Sigma-Aldrich), were used as received.

0.1M Cu:NiO_x (5% Cu) was prepared by dissolving $Ni(NO_3)_2 \cdot 6H_2O$ and $Cu(NO_3)_2 \cdot 3H_2O$ in 2-methoxyethanol:acelyacetone with 9:1 volumetric ratio and sonicated to make sure it is completely dissolved[10] PTAA (Solaris M) solution was prepared with toluene by concentration 8 mg/mL and diluting to 2 mg/mL before the use. The perovskite precursor solution with 1.4M equimolar concentration was prepared with the formula $Cs_{0.15}FA_{0.85}Pb(I_{0.95}Br_{0.05})_3$ using 1290.8 mg PbI_2, 409.3 mg FAI, 89.38 mg CsBr and dissolved in 4:1 volumetric ratio of DMF:DMSO. It was stirred overnight at room temperature in the glovebox before the spin-coating process. PCBM was prepared by dissolving the powder in CB with a concentration of 20 mg/mL, and also stirred overnight at room temperature in the glovebox. The stock solution of PEI was prepared by dissolving PEI in IPA with a concentration of 8 wt% and diluted to 0.1 wt% and stirred overnight before device fabrication.

The hole transporting layer (HTL) made of Cu:NiO_x was coated by static spin-coating in the glovebox with a 1500 rpm and 1500 RPM/s acceleration for 60 s. It was annealed using a two-step method, firstly at 150°C for 5 min in the glovebox, and then at 300°C for 15 min in ambient air to have a complex phase transformation. The HTL passivation layer has been performed using PTAA with spin-coating at 5000 RPM and 5000 RPM/s acceleration for 30 s. It was annealed at 100°C for 10min. For the fabrication of the perovskite layer, spin coating combined with anti-solvent dropping was used. The process started with a 1000 rpm and 200 rpm/s acceleration for 5 s, and then continued at 5000 RPM and 5000 rpm/s acceleration for 30s. At the 15th second of the second step CB was dropped onto the sample to facilitate the formation of the intermediate phase of the perovskite.

The dynamic spin-coating with around 200 µL perovskite precursor solution was used due to the hydrophobic property of PTAA. Subsequently, 110°C annealing process for 20 minutes was used to form the perovskite crystal. The electron transporting later (ETL) was made with PCBM material and spin-coated with a 1000 RPM and 1000 RPM/s acceleration for 30 s. PEI was used as a buffer layer and work-function modifier and spin-coated with at 3000 RPM with 3000 RPM/s acceleration for 30 s. Lastly, 100 nm of silver was thermally evaporated on the top of the samples under pressure lower than 5×10^{-6} mbar to finish the device with an active area of 0.09cm^2. The samples were encapsulated using the UV resin (FMPV® EN-2, FrontMaterials) and covered with 1 mm glass at the top of the active area. To remove any air bubbles the samples were kept 10^{-2} mbar vacuum for 30 min and subsequently cured with UV for two 10 min cycles.

Characterization

Current density (J-V) characterization was performed using an Auto-Lab potentiostat/galvanostat, model PGSTAT204 (Methrohm), driven by the NOVA software (2.1.4 version). VeraSol-2 LED solar simulator was used as illumination source for indoor illumination and degradation. Temperature I-V measurements were performed in N_2 on an Instec Custom-TP102G gas-tight Peltier thermal plated configured with a mK2000 temperature controller. Though the actual intensity of the solar simulator was 1 sun, due to reflection and absorption losses from the stage windows there was a drop in intensity or around 15 %. Therefore, the efficiency measured in the temperature experiment is underestimated around 15 %. The solar cells were equilibrated at each temperature for ~ 4 minutes before measuring.

Indoor degradation was performed by measuring J-V curves every 10 minutes under 1 sun illumination (ISOS-L-1 protocol). Devices were kept at open circuit conditions between measurements.

Characterization of the cell outdoor degradation was done following the ISOS-O-2 stability protocol described by Khenkin et al [18]. Periodic J-V curves were monitored for each cell in an experimental outdoor setting consisting of a dual-axis automatic sun tracker and a National Instruments PXIe-4139 Source Measurement Unit, coupled to a National Instruments PXI-2527 32-channel multiplexer. Between measurements, all cells were kept at open circuit conditions. Solar radiation components (direct, diffuse, and global in both horizontal and 2-axis tracking planes) have been constantly monitored via a Kipp & Zonen Solys2 GPS-based sun tracker equipped with Kipp & Zonen CMP6 and EPLAB SPP pyranometers, together with a Kipp & Zonen CHP1 pyrheliometer. Outdoor weather conditions (temperature, relative humidity, atmospheric pressure, wind data and precipitation) have also been acquired using Alhborn FHAD and Thies Clima sensor modules.

Conclusions

In this work CsFaPbIBr based perovskite solar cells have been characterized in DC at different temperatures. The activation energy, obtained from the dependence of V_{OC} with

ARTICLE | Journal Name

temperature, is very similar to the band gap energy (~1.58 eV), which indicates that the dominant carrier recombination process takes place in the bulk rather than at the perovskite/contact interface. However, at low temperatures, the strong decrease of the FF at high irradiation levels, and the drop of the ideality factor suggest an increase of the recombination at the perovskite/contact. Moreover, at room temperature, the cells show low hysteresis, a good temperature performance, with $T_{PCE} \sim 0$ and good stability after more than 350 h of light cycling. Finally, these devices show a good outdoor performance under extreme Spanish summer conditions with a $T_{80} > 15$ days

Author Contributions

Beatriz Romero: Conceptualization, Investigation, Project administration, Writing-original draft. **Silvia Delgado**: Data curation, Formal analysis, Investigation. **Gonzalo del Pozo**: Data curation, Formal analysis, Investigation. **Pedro Contreras**: Data curation, Formal analysis. **Belén Arredondo**: writing- review & editing, Resources, Funding acquisition. **Diego Martín**: Resources, Funding acquisition, Writing- review & editing. **Damian Glowienka**: Resources, Writing original draft, **Yulia Galagan**: Resources, Funding acquisition.

Conflicts of interest

There are no conflicts to declare.

Acknowledgements

References

1 J. Y. Kim, J.-W. Lee, H. S. Jung, H. Shin and N.-G. Park, *Chem. Rev.*, 2020, **120**, 7867–7918.

2 H. Min, D. Y. Lee, J. Kim, G. Kim, K. S. Lee, J. Kim, M. J. Paik, Y. K. Kim, K. S. Kim, M. G. Kim, T. J. Shin and S. Il Seok, *Nature*, 2021, **598**, 444–450.

3 A. Roy, A. Ghosh, S. Bhandari, S. Sundaram and T. K. Mallick, *Buildings*, 2020, **10**, 129.

4 Y. Tu, J. Wu, G. Xu, X. Yang, R. Cai, Q. Gong, R. Zhu and W. Huang, *Adv. Mater.*, 2021, **33**, 2006545.

5 D.-H. Choi, H.-J. Seok, S.-K. Kim, D.-H. Kim and B. HOU, *Sol. RRL*, , DOI:10.1002/solr.202100660.

6 B. Suarez, V. Gonzalez-Pedro, T. S. Ripolles, R. S. Sanchez, L. Otero and I. Mora-Sero, *J Phys Chem Lett*, 2014, 8.

7 Measuring Aging Stability of Perovskite Solar Cells | Elsevier Enhanced Reader, https://reader.elsevier.com/reader/sd/pii/S2542435118302241?token=1A5F4AC7A5E7BE4E3BF9D8EB1F73FC71826BFB9A008865496157E5D7472A4EAA38FB4229F9DF1237DD3B2957E8DA80F1&originRegion=eu-west-1&originCreation=20221018083854, (accessed 18 October 2022).

8 M. Wang, W. Wang, B. Ma, W. Shen, L. Liu, K. Cao, S. Chen and W. Huang, *Nano-Micro Lett.*, 2021, **13**, 62.

9 Y. Wang, L. Duan, M. Zhang, Z. Hameiri, X. Liu, Y. Bai and X. Hao, *Sol. RRL*, **n/a**, 2200234.

10 D. Głowienka, D. Zhang, F. Di Giacomo, M. Najafi, S. Veenstra, J. Szmytkowski and Y. Galagan, *Nano Energy*, 2020, **67**, 104186.

11 J. Haddad, B. Krogmeier, B. Klingebiel, L. Krückemeier, S. Melhem, Z. Liu, J. Hüpkes, S. Mathur and T. Kirchartz, *Adv. Mater. Interfaces*, 2020, **7**, 2000366.

12 W. Tress, K. Domanski, B. Carlsen, A. Agarwalla, E. A. Alharbi, M. Graetzel and A. Hagfeldt, *Nat. Energy*, 2019, **4**, 568–574.

13 T. Moot, J. B. Patel, G. McAndrews, E. J. Wolf, D. Morales, I. E. Gould, B. A. Rosales, C. C. Boyd, L. M. Wheeler, P. A. Parilla, S. W. Johnston, L. T. Schelhas, M. D. McGehee and J. M. Luther, *ACS Energy Lett.*, 2021, **6**, 2038–2047.

14 W. Tress, M. Yavari, K. Domanski, P. Yadav, B. Niesen, J. P. C. Baena, A. Hagfeldt and M. Graetzel, *Energy Environ. Sci.*, 2018, **11**, 151–165.

15 M. V. Khenkin, E. A. Katz, A. Abate, G. Bardizza, J. J. Berry, C. Brabec, F. Brunetti, V. Bulović, Q. Burlingame, A. Di Carlo, R. Cheacharoen, Y.-B. Cheng, A. Colsmann, S. Cros, K. Domanski, M. Dusza, C. J. Fell, S. R. Forrest, Y. Galagan, D. Di Girolamo, M. Grätzel, A. Hagfeldt, E. von Hauff, H. Hoppe, J. Kettle, H. Köbler, M. S. Leite, S. Liu, Y.-L. Loo, J. M. Luther, C.-Q. Ma, M. Madsen, M. Manceau, M. Matheron, M. McGehee, R. Meitzner, M. K. Nazeeruddin, A. F. Nogueira, Ç. Odabaşı, A. Osherov, N.-G. Park, M. O. Reese, F. De Rossi, M. Saliba, U. S. Schubert, H. J. Snaith, S. D. Stranks, W. Tress, P. A. Troshin, V. Turkovic, S. Veenstra, I. Visoly-Fisher, A. Walsh, T. Watson, H. Xie, R. Yıldırım, S. M. Zakeeruddin, K. Zhu and M. Lira-Cantu, *Nat. Energy*, 2020, **5**, 35–49.

16 M. O. Reese, S. A. Gevorgyan, M. Jørgensen, E. Bundgaard, S. R. Kurtz, D. S. Ginley, D. C. Olson, M. T. Lloyd, P. Morvillo, E. A. Katz, A. Elschner, O. Haillant, T. R. Currier, V. Shrotriya, M. Hermenau, M. Riede, K. R. Kirov, G. Trimmel, T. Rath, O. Inganäs, F. Zhang, M. Andersson, K. Tvingstedt, M. Lira-Cantu, D. Laird, C. McGuiness, S. (Jimmy) Gowrisanker, M. Pannone, M. Xiao, J. Hauch, R. Steim, D. M. DeLongchamp, R. Rösch, H. Hoppe, N. Espinosa, A. Urbina, G. Yaman-Uzunoglu, J.-B. Bonekamp, A. J. J. M. van Breemen, C. Girotto, E. Voroshazi and F. C. Krebs, *Sol. Energy Mater. Sol. Cells*, 2011, **95**, 1253–1267.

17 K. Domanski, B. Roose, T. Matsui, M. Saliba, S.-H. Turren-Cruz, J.-P. Correa-Baena, C. R. Carmona, G. Richardson, J. M. Foster, F. De Angelis, J. M. Ball, A. Petrozza, N. Mine, M. K. Nazeeruddin, W. Tress, M. Grätzel, U. Steiner, A. Hagfeldt and A. Abate, *Energy Env. Sci*, 2017, **10**, 604–613.

18 M. V. Khenkin, A. K. M, I. Visoly-Fisher, Y. Galagan, F. D. Giacomo, B. R. Pątil, G. Sherafatipour, V. Turkovic, H.-G. Rubahn, M. Madsen, T. Merckx, G. Uytterhoeven, J. P. A. Bastos, T. Aernouts, F. Brunetti, M. Lira-Cantu and E. A. Katz, *Energy Environ. Sci.*, 2018, **11**, 739–743.

19 F. Huang, L. Jiang, A. R. Pascoe, Y. Yan, U. Bach, L. Spiccia and Y.-B. Cheng, *Nano Energy*, 2016, **27**, 509–514.

20 P. Calado, A. M. Telford, D. Bryant, X. Li, J. Nelson, B. C. O'Regan and P. R. F. Barnes, *Nat. Commun.*, 2016, **7**, 13831.

21 P. Calado, D. Burkitt, J. Yao, J. Troughton, T. M. Watson, M. J. Carnie, A. M. Telford, B. C. O'Regan, J. Nelson and P. R. F. Barnes, *Phys. Rev. Appl.*, 2019, **11**, 044005.

22 R. García-Rodríguez, A. J. Riquelme, M. Cowley, K. Valadez-Villalobos, G. Oskam, L. J. Bennett, M. J. Wolf, L. Contreras-Bernal, P. J. Cameron, A. B. Walker and J. A. Anta, *Energy Technol.*, **n/a**, 2200507.

23 D. Glowienka and Y. Galagan, *Adv. Mater.*, 2022, **34**, 2105920.

24 D. Głowienka, T. Miruszewski and J. Szmytkowski, *Solid State Sci.*, 2018, **82**, 19–23.